Supplementary Material for:

Air-sea coupling shapes North American hydroclimate response to ice sheets during the Last Glacial Maximum

Dillon J. Amaya[1], Alan M. Seltzer[2], Kristopher B. Karnauskas[1,3], Juan M. Lora[4], X. Zhang[5], and Pedro N. DiNezio[3]

[1]Cooperative Institute for Research in Environmental Sciences, University of Colorado Boulder

[2]Woods Hole Oceanographic Institution

[3]Department of Atmospheric and Oceanic Sciences, University of Colorado Boulder

[4]Department of Earth and Planetary Sciences, Yale University

[5]Department of Earth and Planetary Sciences, Johns Hopkins University

Corresponding author: Dillon J. Amaya, dillon.amaya@colorado.edu, 816-916-8348

This PDF file includes:

S1 Equilibrium mixed layer heat budget

S1.1 Heat budget derivation

To diagnose the physical processes that drive the main features of the sea surface temperature (SST) anomaly patterns discussed in this study, we conduct a mixed layer heat budget analysis following Xie et al. (2010). The mixed layer heat budget can be written as:

$$\rho c_p H \frac{\partial SST'}{\partial t} = Q'_{SW} + Q'_{LW} + Q'_{SH} + Q'_{LH} + O' \quad \text{(S1)}$$

where ρ is ocean density, c_p is the specific heat capacity of seawater, H is the ocean mixed layer depth, and SST' is the mixed layer temperature (estimated here as SST). Primes denote differences between our perturbed simulations (e.g., WM or GM) and the CTL simulations. The combination of terms on the left-hand side (LHS) represent time variations in the mixed layer heat storage, which is very close to zero in the annual mean of our equilibrium climate simulations (not shown). The terms on the right-hand side (RHS) represent the drivers of those changes (positive values = SST warming), which include net surface shortwave radiation (Q'_{SW}), net surface longwave radiation (Q'_{LW}), sensible (Q'_{SH}) and latent (Q'_{LH}) heat fluxes, and the heat flux due to ocean dynamics (O') calculated as a residual.

We aim to rewrite Eq. (S1) as a diagnostic equation for SST anomalies between our equilibrium simulations due to the dependency of the latent heat flux on SST (Hwang et al., 2017; Jia and Wu, 2013; Zhang et al., 2020). To get there, we begin with the bulk formula for the latent heat flux:

$$Q_{LH} = -L_v c_E \rho_a W [q_s(SST) - q_a] \quad \text{(S2)}$$

where L_v is the latent heat of vaporization, c_E is the transfer coefficient, ρ_a is the near-surface air density, W is the surface wind speed, and q_a is the specific humidity of air above the sea surface. The near-surface specific humidity of air is defined as:

$$q_a = RH_0 q_s(SST + \Delta T) \tag{S3}$$

where RH_0 is the relative humidity at the sea surface, and $\Delta T = T_a - SST$ is the near-surface temperature gradient. Using the Clausius-Clapeyron equation, Eq. (S3) can be rewritten as:

$$q_a = RH_0 q_s(SST) e^{\alpha \Delta T} \tag{S4}$$

where $\alpha = \frac{L_v}{R_v T^2} \approx 0.06\ \mathrm{K}^{-1}$. Plugging Eq. (S4) into Eq. (S2), we get:

$$Q_{LH} = -L_v c_E \rho_a W (1 - RH_0 e^{\alpha \Delta T}) q_s(\mathrm{SST}) \tag{S5}$$

Following Jia and Wu (2013), anomalies of Q_{LH} can be linearized such that:

$$Q'_{LH} = \frac{\delta Q_{LH}}{\delta SST} SST' + \frac{\delta Q_{LH}}{\delta W} W' + \frac{\delta Q_{LH}}{\delta RH_0} RH'_0 + \frac{\delta LH}{\delta \Delta T} \Delta T' \tag{S6}$$

The last three terms on the RHS represent contributions to the total latent heat flux from near-surface wind speed, near-surface relative humidity, and air-sea temperature contrasts, respectively. These terms can be represented as:

$$Q_{LH,w} = \frac{\delta Q_{LH}}{\delta W} W' = \overline{Q_{LH}} \frac{W'}{\overline{W}}, \tag{S7}$$

$$Q_{LH,RH} = \frac{\delta Q_{LH}}{\delta RH_0} RH'_0 = -\frac{\overline{Q_{LH}} RH'_0}{e^{\alpha \overline{\Delta T}} - \overline{RH_0}}, \tag{S8}$$

$$Q_{LH,\Delta T} = \frac{\delta Q_{LH}}{\delta \Delta T} \Delta T' = \frac{\alpha \overline{Q_{LH}}\, \overline{RH_0} \Delta T'}{e^{\alpha \overline{\Delta T}} - \overline{RH_0}}, \tag{S9}$$

while the first term on the RHS of Eq. (S6) represents SST damping from Newtonian cooling:

$$Q_{LH,SST} = \frac{\delta Q_{LH}}{\delta SST} SST' = \alpha \overline{Q_{LH}} SST' \tag{S10}$$

where overbars denote the climatological mean. By substituting Eq. (S10) into Eq. (S1) and solving, we arrive at a diagnostic equation for SST':

$$SST' = -\frac{Q'_{SW} + Q'_{LW} + Q'_{SH} + Q'_{LH,w} + Q'_{LH,RH} + Q'_{LH,\Delta T} + O'}{\alpha \overline{Q_{LH}}} \tag{S11}$$

Finally, Eq. (S11) can be rewritten to show how each forcing term contributes to SST':

$$SST' = SST'_{SW} + SST'_{LW} + SST'_{SH} + SST'_O + SST'_{LH,w} + SST'_{LH,RH} + SST'_{LH,\Delta T} \tag{S12}$$

where:

$$SST'_{SW} = -\frac{Q'_{SW}}{\alpha\overline{Q_{LH}}}, \tag{S13}$$

$$SST'_{LW} = -\frac{Q'_{LW}}{\alpha\overline{Q_{LH}}}, \tag{S14}$$

$$SST'_{SH} = -\frac{Q'_{SH}}{\alpha\overline{Q_{LH}}}, \tag{S15}$$

$$SST'_{Ocn} = -\frac{O'}{\alpha\overline{Q_{LH}}}, \tag{S16}$$

$$SST'_{LH,w} = -\frac{Q'_{LH,w}}{\alpha\overline{Q_{LH}}} = -\frac{W'}{\alpha\overline{W}}, \tag{S17}$$

$$SST'_{LH,RH} = -\frac{Q'_{LH,RH}}{\alpha\overline{Q_{LH}}} = -\frac{RH'_0}{\alpha(e^{\alpha\overline{\Delta T}} - \overline{RH_0})}, \tag{S18}$$

$$SST'_{LH,\Delta T} = -\frac{Q'_{LH,\Delta T}}{\alpha\overline{Q_{LH}}} = -\frac{\overline{RH_0}\,\Delta T'}{e^{\alpha\overline{\Delta T}} - \overline{RH_0}}, \tag{S19}$$

S1.2 Cloud parameters

The contribution of surface shortwave radiation to SST' can be further decomposed as:

$$SST'_{SW} = SST'_{SW,Cld} + SST'_{SW,Clr} \tag{S21}$$

where $SST'_{SW,Cld}$ is the SST contribution from the changes in shortwave cloud radiative forcing and $SST'_{SW,Clr}$ is the SST contribution from changes in shortwave radiation at the surface under a clear sky. The terms in Eq. (S21) are shown in Figure 7 of the main text, where the LHS is Eq. (S13) and the RHS terms are:

$$SST'_{SW,Clr} = -\frac{Q'_{SW,Clr}}{\alpha\overline{Q_{LH}}} \tag{S22}$$

$$SST'_{SW,Cld} = \frac{Q'_{SW} - Q'_{SW,Clr}}{\alpha\overline{Q_{LH}}} \tag{S23}$$

The cloud forced cooling seen in WM_{DOM} and WM_{AGCM} is closely mirrored by increases in summertime low cloud fraction throughout the North Pacific (Figure 8a,d). Following Scott et

al. (2020), we diagnose the physical drivers of these low cloud changes by comparing to summertime averaged Estimated Inversion Strength (EIS) and 700 mb relative humidity (RH) anomalies in each of our simulations (Figures 8b-c and 8e-f). The EIS is calculated as:

$$EIS = LTS - \Gamma_m^{850}(z_{700} - LCL) \quad \text{(S24)}$$

where *LTS* is the lower tropospheric stability and is equal to the difference between the air temperature at 700 mb and the surface temperature, z_{700} is the height of the 700 mb pressure surface, *LCL* is the lifted condensation level (i.e., the cloud bottom) calculated following Georgakakos and Bras (1984), and Γ_m^{850} is the moist adiabatic lapse rate at 850 mb calculated as:

$$\Gamma_m^{850} = \frac{g}{c_{pa}}\left[1 - \frac{1 + {L_v w_s^{850}}/{R_d T^{850}}}{1 + {L_v^2 w_s^{850}}/{c_{pa} R_v T^{850^2}}}\right] \quad \text{(S25)}$$

where w_s^{850} and T^{850} are the saturation mixing ratio and air temperature at 850 mb, respectively, and R_d and $R_v$are the gas constants for dry air and water vapor, respectively, and c_{pa} is the specific heat capacity of air at constant pressure. The EIS (˚C) is a measure of the strength of the temperature inversion above the marine boundary layer (MBL). Positive EIS values correspond to a stronger inversion and reduced mixing between the moist MBL and the drier free troposphere and are therefore highly correlated with increases in low cloud fraction Wood and Bretherton (2006).

S1.3 Ekman heat transport

Annual mean Ekman heat advection anomalies for GM and WM dynamical ocean model (DOM) simulations are shown in Figure S6. Anomalous Ekman heat advection (Q'_{ek}) is calculated following Alexander and Scott (2008):

$$Q'_{ek} = \frac{c_p}{f}\left(\tau_x \frac{\delta SST}{\delta y} - \tau_y \frac{\delta SST}{\delta x}\right) \quad \text{(S20)}$$

where f is the Coriolis parameter, τ_x and τ_y are the zonal and meridional surface wind stress, and $\frac{\delta SST}{\delta x}$ and $\frac{\delta SST}{\delta y}$ are the zonal and meridional SST gradients, which we use to estimate the horizontal temperature gradients within the Ekman layer.

S1.4 Heat budget interpretation

The SST budgets shown in Figures S4 and S5 use Eqs. (S12-S19). As this heat budget is only valid for the upper ocean, the budget terms are only plotted for grid cells that are 100% ocean for the entire year. Grid cells that experience any fraction of seasonal sea ice are masked out. Note that these budgets are not expected to close exactly. In particular, this heat budget decomposition assumes a local quasi-equilibrium between the surface temperature and near-surface air temperature. Therefore, SST' in Eq. (S12) may have larger errors in regions with strong boundary layer temperature advection, which may occur near areas with large surface temperature gradients (e.g., near sea ice, western boundary currents, etc.). There may be additional errors brought on from non-linearities in the surface heat flux terms that are not captured in our analysis.

Additionally, we note that this heat budget decomposition can only be applied for annual mean data. This is due to the necessary assumption that the mixed layer heat storage (LHS, Eq. S1) is close to zero, which is only true in the annual mean of our equilibrium climate simulations. Seasonal averages of equilibrium mixed layer heat storage are not required to be close to zero as they may be balanced by opposite signed changes in other seasons. Despite these caveats, our annual mean heat budget is a useful qualitative tool to identify the dominant SST-forcing terms, which when combined with other seasonally averaged climate anomalies (as in Figure 7g), can provide clues for the specific ocean-atmosphere interactions at play.

S2 Influence of LGM greenhouse gas forcing

While subpolar warming is key in shaping the overall wintertime North Pacific atmospheric circulation response in our GM_{DOM} simulation, this SST pattern may be less apparent when other LGM boundary conditions are also considered. For example, it may be possible that the global cooling associated with reduced LGM GHGs is enough to offset the subpolar warming seen in GM_{DOM}, thus making it possible for mechanical ice sheet forcing alone to drive the expected hydroclimate response. To test this, we estimate the climate response to reduced LGM GHGs using two methods: (1) A fully coupled simulation that is identical to the pre-industrial simulation except with GHGs set to PMIP3 LGM levels (referred to as LGM_{GHG}) and (2) The difference of LGM_{Full} and our WM_{DOM} simulation. The first method estimates the impact of reduced GHGs relative to modern day topography. The second method estimates the impact of reduced GHGs (with some relatively minor contributions from changes in orbital forcing) relative to LGM topography.

Regardless of the method, we find that reducing GHGs to LGM levels does not produce a North Pacific jet shift or a western North America hydroclimate response that is consistent with LGM_{Full} (Figure S7a-d). Even if we assume that the climate impacts of ice sheet topography and reduced LGM GHGs are, to first order, linearly additive (as supported by Zhu and Poulsen, (2021)), their combined effects are still unable to reproduce the expected atmospheric circulation or hydroclimate response (Figure S7e-f). This is because reducing GHGs does not significantly alter the anomalous meridional temperature gradient set up by the direct mechanical ice sheet forcing in GM_{DOM}. Instead, reducing GHGs merely cools the North Pacific fairly uniformly (not shown), which does not significantly impact the North Pacific jet stream. This is consistent with previous studies that showed that lowered GHGs can indeed influence Northern Hemisphere

stationary waves, but that this effect is minor relative to other LGM boundary conditions (Broccoli and Manabe, 1987; Masson-Delmotte et al., 2006).

S3 Additional AGCM experiments

In order to isolate the contribution of SST-forcing to the overall atmospheric circulation anomalies seen in coupled simulations, we conducted a series of additional CAM5 simulations (referred to as WM-SST) forced at the lower boundary with the long-term monthly mean SST output from the WM_{DOM} experiment (Figure 6a). Sea ice fraction was prescribed following a repeated seasonal cycle from the CTL_{DOM} simulation. Separate experiments were conducted by forcing CAM5 with WM_{DOM} SSTs (a) globally, (b) in the tropics-only (20˚S-20˚N), (c) in the North Pacific-only (>30˚N), and (d) in the Northern extratropics (>30˚N, all longitudes). Grid points not prescribed with WM_{DOM} SSTs were set to the CTL SST seasonal cycle. Each simulation was integrated for 40 years. Due to the short decorrelation timescale of the atmosphere, each year of these simulations was treated as a separate ensemble member. All anomalies are relative to a WM-SST control experiment forced with CTL_{DOM} SSTs globally. Results are shown for the boreal winter (December-February) ensemble average within each experiment (Figure 6).

Table S1 List of PMIP3 models used in this study. Where a model offered multiple ensemble members, only the first ensemble member was used for analysis.

Institution	Model	Resolution (lat x lon)
National Center for Atmospheric Research	CCSM4	0.94˚ x 1.25˚
Centre National de Recherches M´et´eorologiques/Centre Europ´een de Recherche et de Formation Avanc´ee en Calcul Scientifique	CNRM-CM5	1.4˚ x 1.4˚
LASG, Institute of Atmospheric Physics, Chinese Academy of Sciences and CESS, Tsinghua University	FGOALS-g2	2.8˚ x 2.8˚
NASA Goddard Institute for Space Studies	GISS-E2-R	2.0˚ x 2.5˚
Institut Pierre-Simon Laplace	IPSL-CM5A-LR	1.9˚ x 3.75˚
Japan Agency for Marine-Earth Science and Technology, Atmosphere and Ocean Research Institute (The University of Tokyo), and National Institute for Environmental Studies	MIROC-ESM	2.8˚ x 2.8˚
Max Planck Institute for Meteorology	MPI-ESM-P	1.87˚ x 1.87˚
Meteorological Research Institute	MRI-CGCM3	1.12˚ x 1.12˚

Table S2 Compilation of western North American LGM minus pre-industrial precipitation difference estimates from (second column) proxy records and (third column) our CESM1 LGM_{Full} simulation. Proxy locations are in the first column. Paired CESM1 data is from the nearest grid cell. Proxy estimates are modified from Lora et al. (2017). Superscripts in the second column denote the citation for each respective proxy estimate. Full references are in main text.

Location	ΔP, Proxy Estimates (mm day^{-1})	ΔP, CESM1 LGM_{Full} - CTL (mm day^{-1})
47˚N, 123˚W	-3.4 ± 0.2[1]	-1.2
45˚N, 123˚W	-2.6 ± 0.2[1]	-0.6
45˚N, 121˚W	-0.5 ± 0.2[1]	-0.4
41˚N, 121˚W	0.2 ± 0.1[2]	0.3
41˚N, 115˚W	-0.0 ± 0.2[3]	0.2
41˚N, 113˚W	1.1 ± 0.4[4]	0.2
41˚N, 111˚W	0.3 ± 0.7[4]	0.0
39˚N, 115˚W	0.2 ± 0.3[1,3]	0.2
37˚N, 119˚W	0.3 ± 0.3[3]	1.7
37˚N, 117˚W	0.6 ± 0.2[1,3,5]	0.6
37˚N, 115˚W	0.0 ± 0.2[1]	0.3
37˚N, 111˚W	0.5 ± 0.2[1]	0.1
37˚N, 109˚W	-0.1 ± 0.3[1]	0.1
35˚N, 111˚W	-0.7 ± 0.4[1]	0.3
35˚N, 109˚W	2.0 ± 0.3[1]	0.3
33˚N, 109˚W	0.7 ± 0.1[1]	0.4

[1]Bartlein et al. (2011), [2]Ibarra et al. (2014), [3]Maher et al. (2014), [4]Lemons et al. (1996), [5]Thompson et al. (1999)

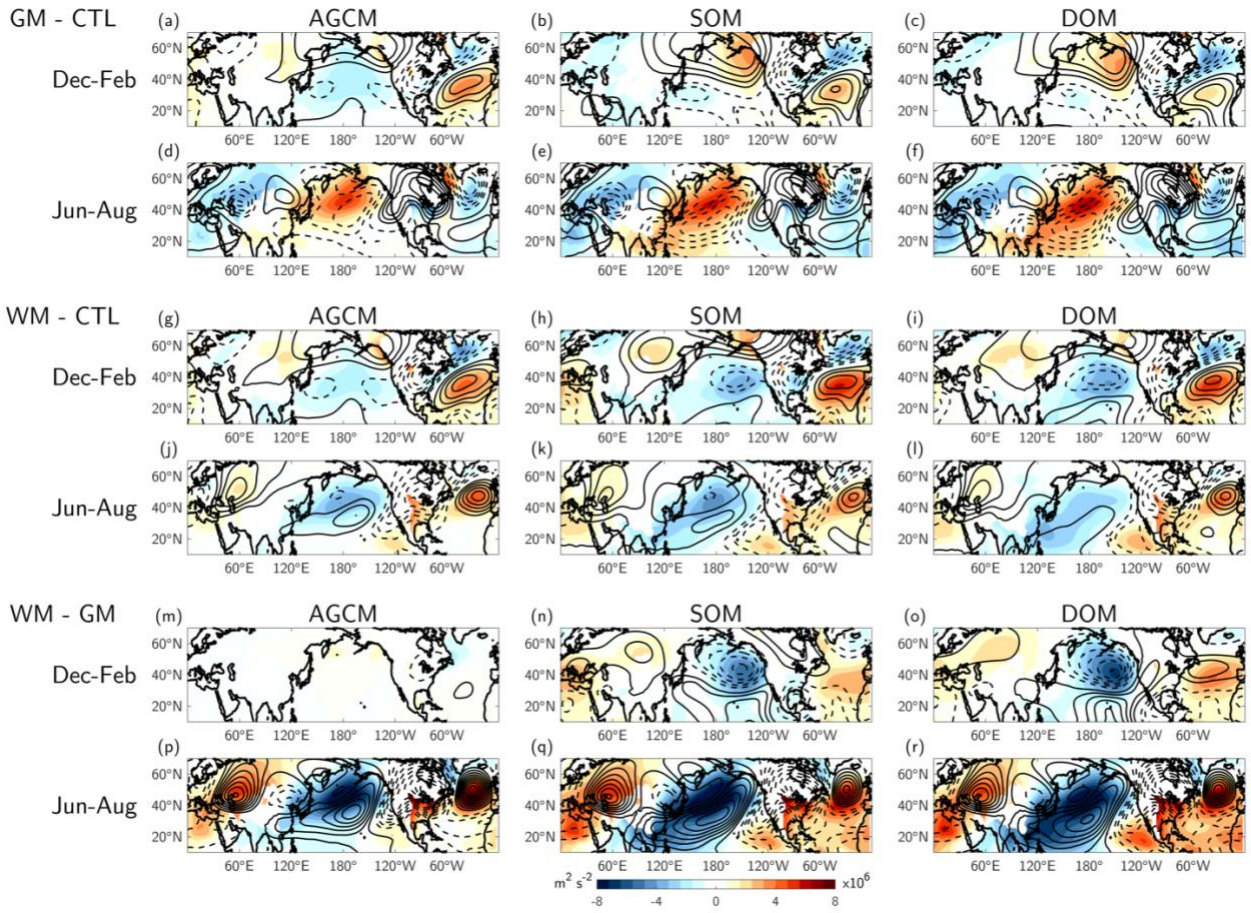

Figure S1 Single forcing North Pacific circulation response. Geostrophic streamfunction anomalies ($m^2\ s^{-2}$) at 850 mb (shading) and 200 mb (black contours) in the GM minus CTL AGCM (left column), SOM (middle column), and DOM (right column) ocean configurations, averaged for (a)-(c) December-February and (d)-(f) June-August. Solid (dashed) black contours denote positive (negative) values. Black contour interval is $2x10^6\ m^2\ s^{-2}$ starting at $2x10^6\ m^2\ s^{-2}$.

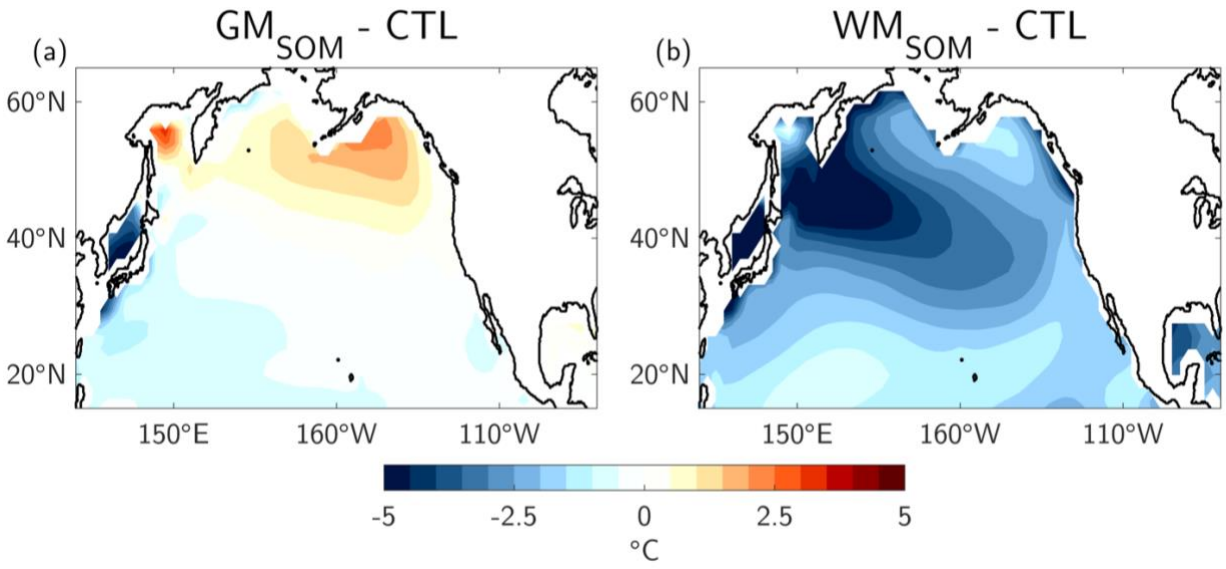

Figure S2 Simulated ocean temperature response. Difference maps of annual mean SSTs (˚C) in (a) GM_{SOM} minus CTL and (b) WM_{SOM} minus CTL.

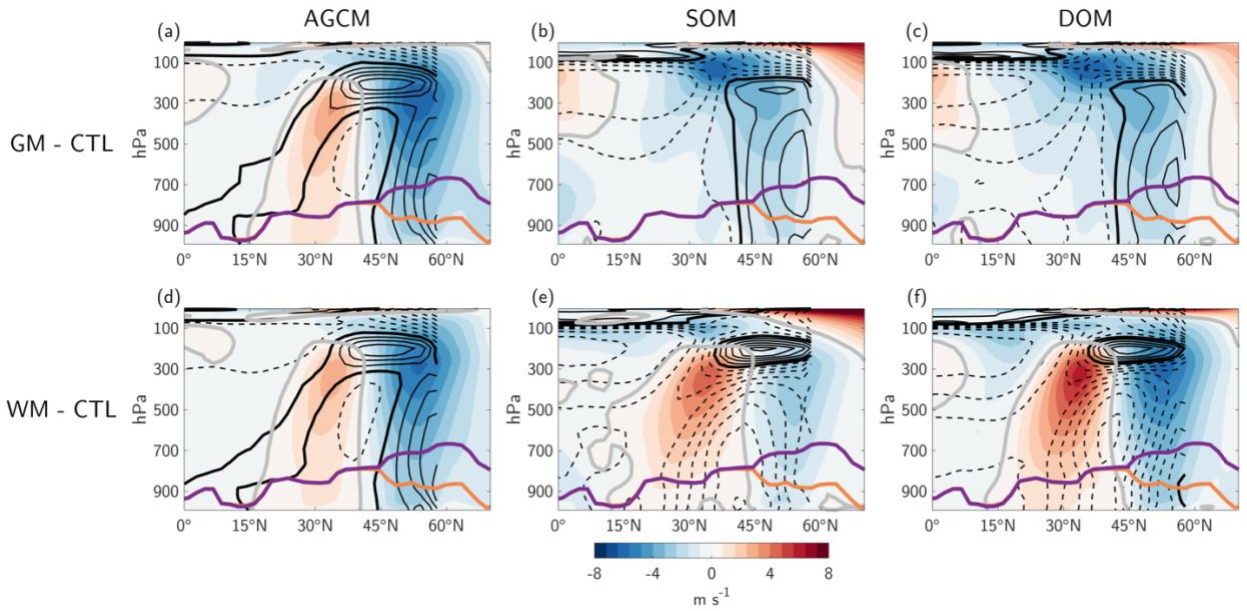

Figure S3 North Pacific wind and temperature response. Latitude-height cross-section of boreal winter (December-February) zonal wind (shading; m s^{-1}) and air temperature anomalies (black contours; ˚C) in (a)-(c) each GM and (d)-(f) each WM simulation, zonally averaged over the Pacific basin (120˚E-110˚W). Temperature values are only averaged over grid cells that are 100% ocean during boreal winter (i.e., excluding grid cells with land or seasonal sea ice). Purple and orange contours roughly outline the profile of North American topography at each latitude (i.e., as if looking westward from the Atlantic Ocean) for LGM and CTL, respectively. Solid (dashed) black contours denote positive (negative) values. Black contour interval is 0.5˚C starting at 0˚C (thick black contour). Thick gray contour marks the 0 m s^{-1} zonal wind anomaly contour.

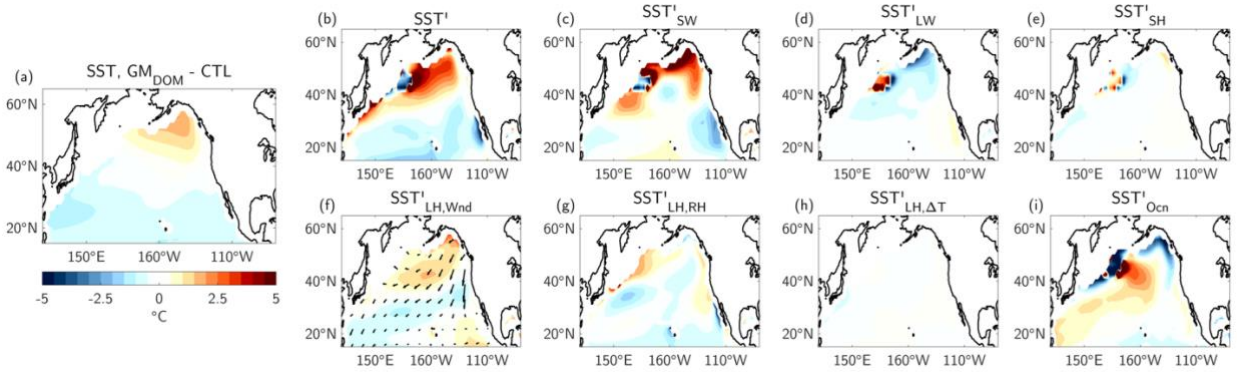

Figure S4 GM$_{DOM}$ mixed layer heat budget. (a) Difference map of annual mean GM$_{DOM}$ minus CTL SSTs (˚C). (b)-(i) Terms of the mixed layer heat budget outlined in Eq. (S12). (b) Sum of the forcing terms, which includes contributions from (c) surface shortwave radiation, (d) surface longwave radiation, (e) the sensible heat flux, latent heat fluxes from changes in (f) wind-speed, (g) relative humidity, and (h) the air-sea temperature difference, and (i) ocean dynamical adjustments calculated as a residual. Arrows in (f) are the corresponding surface wind stress anomalies. Note that values are only shown for grid cells that are 100% ocean for the entire year (see above text on heat budget for more details).

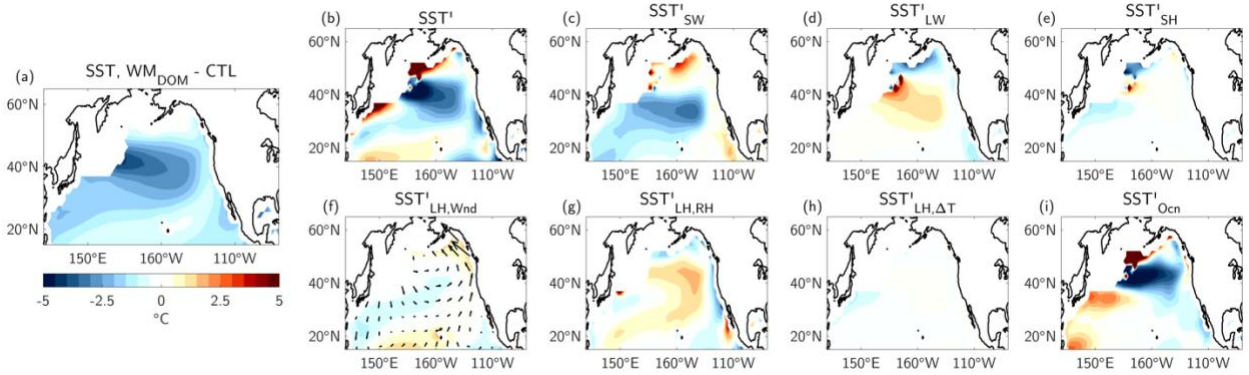

Figure S5 WM$_{DOM}$ mixed layer heat budget. Same as Figure S4, but calculated for the WM$_{DOM}$ simulation.

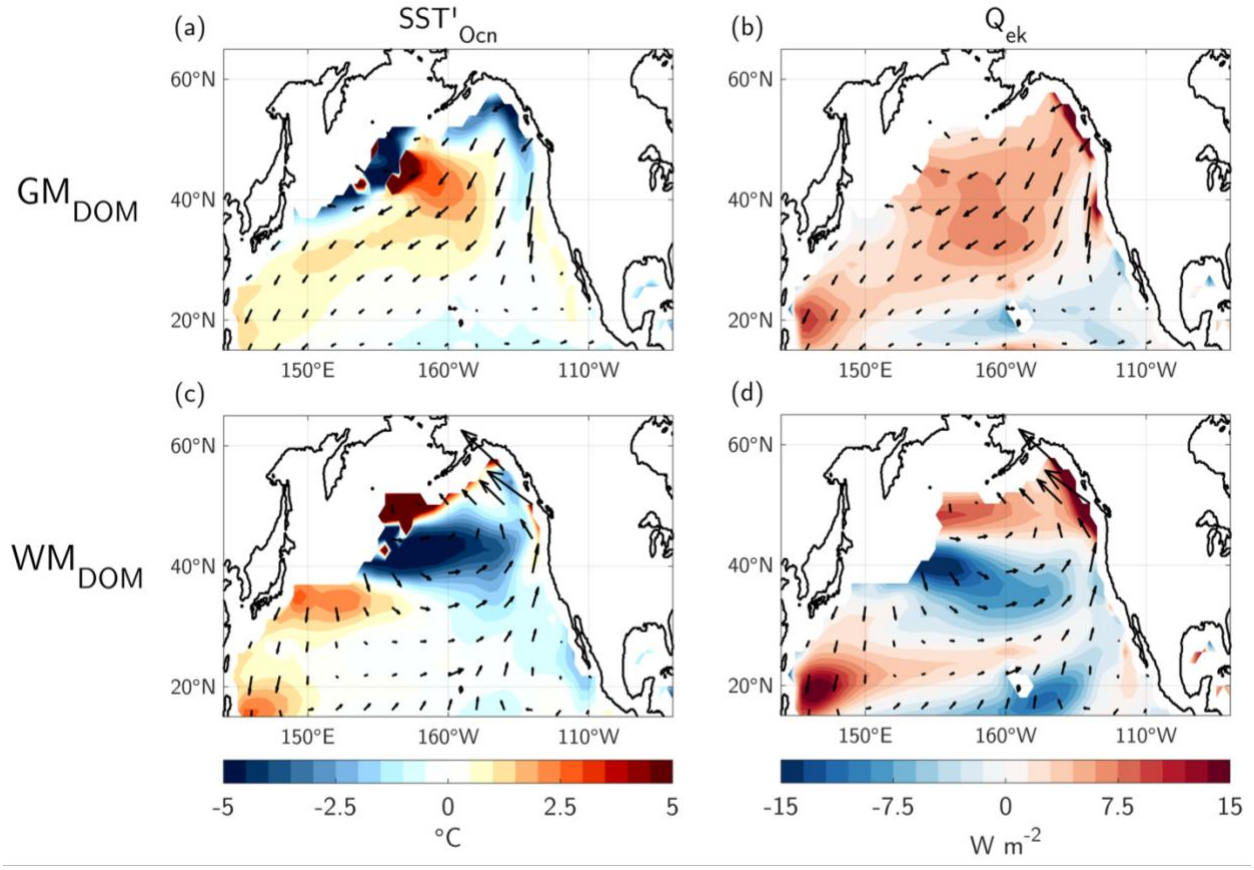

Figure S6 Ocean circulation heat budget terms. (left column) Contribution of ocean circulation changes (SST'_{Ocn}; ˚C) to annual mean SST anomalies and (right column) anomalous Ekman head advection (Q'_{ek}; W m^{-2}) in (a)-(b) GM_{DOM} minus CTL and (c)-(d) WM_{DOM} minus CTL. Arrows show the corresponding annual mean surface wind stress anomalies.

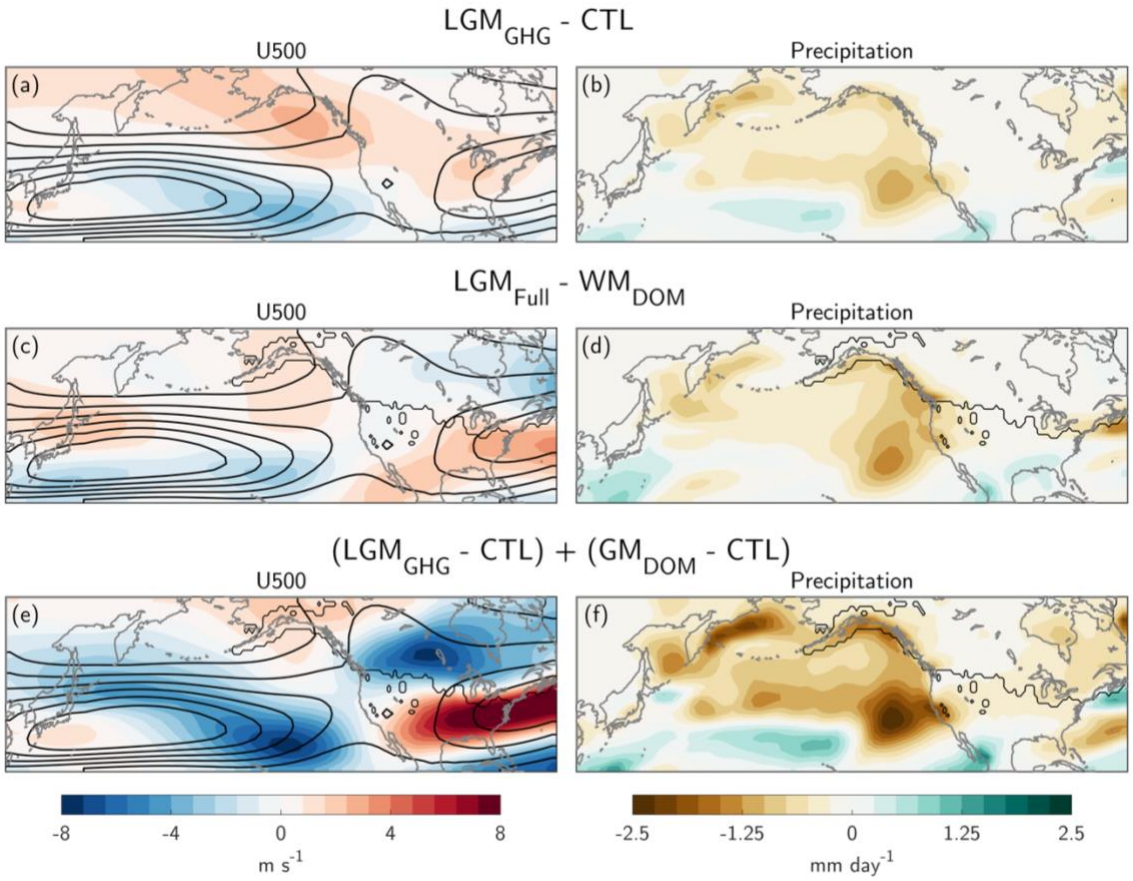

Figure S7 Difference maps of LGM_{GHG} minus CTL (a) 500 mb zonal wind (U500; m s^{-1}) and (b) precipitation (mm day^{-1}) averaged during boreal winter (December-February). (c)-(d) As in (a)-(b), but for LGM_{Full} minus WM_{DOM}. (e)-(f) As in (a)-(b), but for the sum of LGM_{GHG} minus CTL and GM_{DOM} minus CTL. Thick black contours in (a) show wintertime U500 climatology in the pre-industrial control (contour interval is 5 m s^{-1} with max value of 30 m s^{-1}). Thin black contour in (c)-(f) marks approximate ice sheet edge at the LGM.

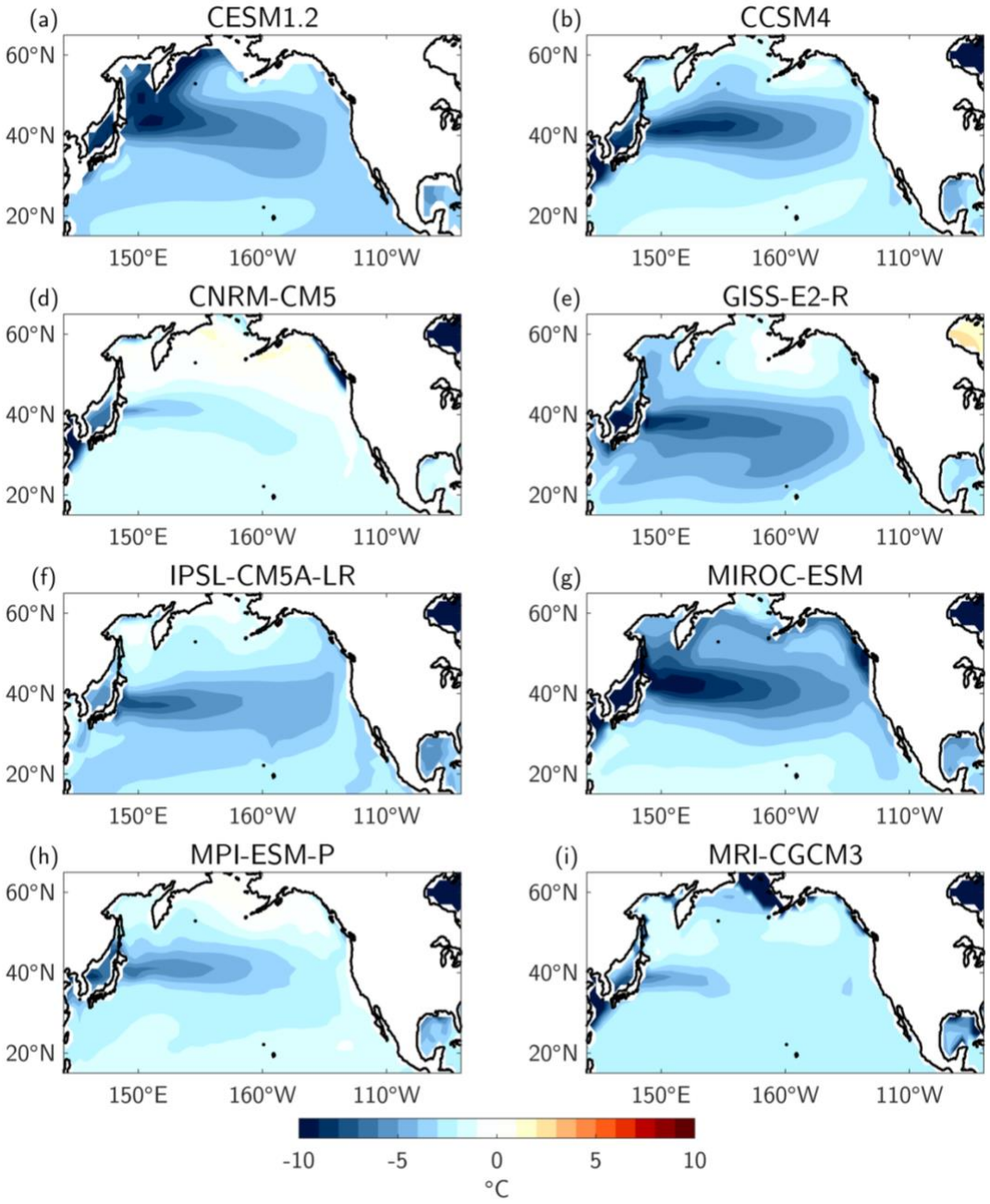

Figure S8 Difference maps of annual mean SSTs (˚C) in (a) our CESM1 LGM_{Full} minus CTL, (b)-(i) the seven LGM_{Full} PMIP3 simulations minus their respective pre-industrial control simulations. The specifications for each PMIP3 model shown here are outlined in Table S1.

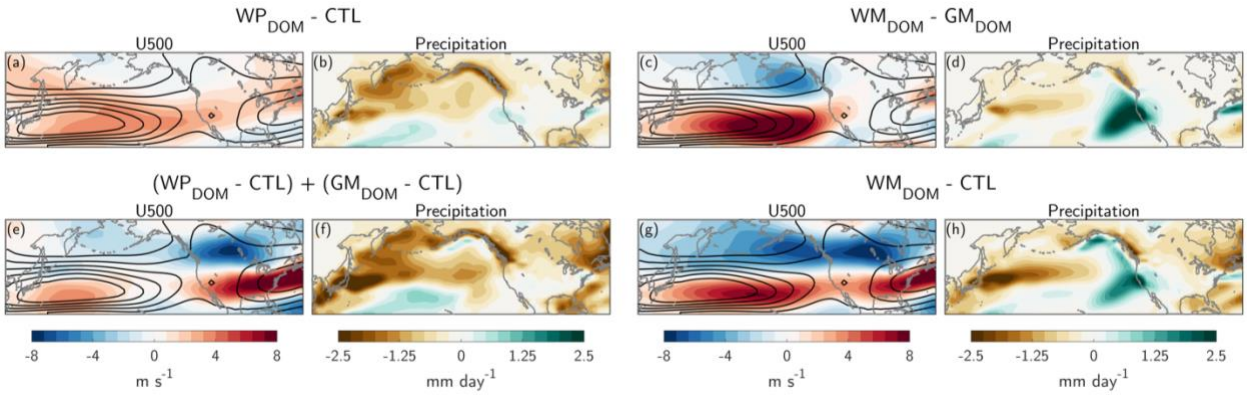

Figure S9 Difference maps of 500mb zonal winds (U500; m s^{-1}) and precipitation (mm day^{-1}) anomalies averaged during boreal winter (December-February). Top row: impact of ice sheet albedo as estimated by (a)-(b) WP_{DOM} anomalies and (c)-(d) WM_{DOM} minus GM_{DOM}. Bottom row: combined impact of ice sheet albedo and ice sheet topography as estimated by (e)-(f) the sum of WP_{DOM} and GM_{DOM} anomalies and (g)-(h) WM_{DOM} anomalies. Thick black contours in zonal wind plots show wintertime U500 climatology in the pre-industrial control (contour interval is 5 m s^{-1} with max value of 30 m s^{-1}).

References

Alexander, M.A., Scott, J.D., 2008. The role of Ekman Ocean heat transport in the northern hemisphere response to ENSO. J. Clim. 21, 5688–5707. https://doi.org/10.1175/2008JCLI2382.1

Broccoli, A.J., Manabe, S., 1987. The influence of continental ice, atmospheric CO2, and land albedo on the climate of the last glacial maximum. Clim. Dyn. 1, 87–99. https://doi.org/10.1007/BF01054478

Georgakakos, K.P., Bras, R.L., 1984. A hydrologically useful station precipitation model: 1. Formulation. Water Resour. Res. 20, 1585–1596. https://doi.org/10.1029/WR020i011p01585

Hwang, Y.T., Xie, S.P., Deser, C., Kang, S.M., 2017. Connecting tropical climate change with Southern Ocean heat uptake. Geophys. Res. Lett. 44, 9449–9457. https://doi.org/10.1002/2017GL074972

Jia, F., Wu, L., 2013. A study of response of the equatorial pacific SST to doubled-CO2 forcing in the coupled CAM-1.5-layer reduced-gravity ocean model. J. Phys. Oceanogr. 43, 1288–1300. https://doi.org/10.1175/JPO-D-12-0144.1

Masson-Delmotte, V., Kageyama, M., Braconnot, P., Charbit, S., Krinner, G., Ritz, C., Guilyardi, E., Jouzel, J., Abe-Ouchi, A., Crucifix, M., Gladstone, R.M., Hewitt, C.D., Kitoh, A., LeGrande, A.N., Marti, O., Merkel, U., Motoi, T., Ohgaito, R., Otto-Bliesner, B., Peltier, W.R., Ross, I., Valdes, P.J., Vettoretti, G., Weber, S.L., Wolk, F., Yu, Y., 2006. Past and future polar amplification of climate change: Climate model intercomparisons and ice-core constraints. Clim. Dyn. 26, 513–529. https://doi.org/10.1007/s00382-005-0081-9

Scott, R.C., Myers, T.A., Norris, J.R., Zelinka, M.D., Klein, S.A., Sun, M., Doelling, D.R., 2020. Observed sensitivity of low-cloud radiative effects to meteorological perturbations over the

global oceans. J. Clim. 33, 7717–7734. https://doi.org/10.1175/JCLI-D-19-1028.1

Wood, R., Bretherton, C.S., 2006. On the relationship between stratiform low cloud cover and lower-tropospheric stability. J. Clim. 19, 6425–6432. https://doi.org/10.1175/JCLI3988.1

Xie, S.P., Deser, C., Vecchi, G.A., Ma, J., Teng, H., Wittenberg, A.T., 2010. Global warming pattern formation: Sea surface temperature and rainfall. J. Clim. 23, 966–986. https://doi.org/10.1175/2009JCLI3329.1

Zhang, X., Deser, C., Sun, L., 2020. Is there a tropical response to recent observed Southern Ocean cooling? Geophys. Res. Lett. https://doi.org/10.1029/2020GL091235

Zhu, J., Poulsen, C.J., 2021. Last Glacial Maximum (LGM) climate forcing and ocean dynamical feedback and their implications for estimating climate sensitivity. Clim. Past 17, 253–267. https://doi.org/10.5194/cp-17-253-2021